

Synthesis, Cation Ordering, and Magnetic Properties of the $(\text{Sb}_{1-x}\text{Pb}_x)_2(\text{Mn}_{1-y}\text{Sb}_y)\text{O}_4$ Solid Solutions with the Sb_2MnO_4 -Type Structure

Artem M. Abakumov,* Marina G. Rozova, and Evgeny V. Antipov

Department of Chemistry, Moscow State University, Moscow 119992, Russia

Joke Hadermann and Gustaaf Van Tendeloo

EMAT, University of Antwerp, Groenenborgerlaan 171, B-2020 Antwerp, Belgium

Maxim V. Lobanov and Martha Greenblatt

Department of Chemistry, Rutgers University, Piscataway, New Jersey 08854

Mark Croft

Department of Physics and Astronomy, Rutgers University, Piscataway, New Jersey 08854

Eugene V. Tsiper

School of Computational Sciences, George Mason University, Fairfax, Virginia 22030, and Center for Computational Material Science, Naval Research Laboratory, Washington, DC 20375

Anna Llobet, Konstantin A. Lokshin, and Yusheng Zhao

LANSCE-12, Los Alamos National Laboratory, Los Alamos, New Mexico 87544

Received July 24, 2004. Revised Manuscript Received December 3, 2004

Single phase $(\text{Sb}_{1-x}\text{Pb}_x)_2(\text{Mn}_{1-y}\text{Sb}_y)\text{O}_4$ ($0.0 \leq x \leq 0.608$, $0.0 \leq y \leq 0.372$) samples with the Sb_2MnO_4 -type structure were prepared at 650 °C by solid-state reaction in evacuated sealed silica tubes. A replacement of Sb by Pb results in the oxidation of Sb^{3+} to Sb^{5+} , which in turn replaces Mn^{2+} cations in octahedrally coordinated positions within the infinite rutile-type chains. The crystal structures of $\text{Pb}_{0.44}\text{Sb}_{1.64}\text{Mn}_{0.92}\text{O}_4$, $\text{Pb}_{0.75}\text{Sb}_{1.48}\text{Mn}_{0.77}\text{O}_4$, $\text{Pb}_{1.07}\text{Sb}_{1.26}\text{Mn}_{0.67}\text{O}_4$, and $\text{Pb}_{1.186}\text{Sb}_{1.175}\text{Mn}_{0.639}\text{O}_4$ were refined from X-ray powder diffraction data. Increasing the Pb content leads to a decrease of the a parameter from $a = 8.719(2)$ Å to $a = 8.6131(8)$ Å and to an increase of the c parameter from $c = 5.999(2)$ Å to $c = 6.2485(7)$ Å (for Sb_2MnO_4 and $\text{Pb}_{1.216}\text{Sb}_{1.155}\text{Mn}_{0.628}\text{O}_4$, respectively). This occurs due to increasing average cation size at the Pb/Sb position and decreasing cation size at the Mn/Sb position that leads to strong deformation of the (Mn/Sb) O_6 octahedra. Starting from the $\text{Pb}_{0.75}\text{Sb}_{1.48}\text{Mn}_{0.77}\text{O}_4$ composition a modulated structure with $\mathbf{q} = \gamma c^*$ was observed by electron diffraction. High-resolution electron microscopy observations revealed that Mn and Sb ions order forming layers of octahedrally coordinated positions filled either by Mn^{2+} or by Sb^{5+} cations and alternating along the c axis. The dilution of the magnetic Mn^{2+} cations by nonmagnetic Sb^{5+} entities leads to a suppression of the antiferromagnetic intrachain interaction and disappearance of long-range magnetic order at high doping level. At $T = 20$ K the A_{xy} spin component was found to be dominant in the AFM structure of the $\text{Pb}_{0.44}\text{Sb}_{1.64}\text{Mn}_{0.92}\text{O}_4$ sample by neutron diffraction.

1. Introduction

The complex transition metal oxides built up of chains of metal–oxygen polyhedra deserve considerable attention due to interesting magnetic behavior driven by one-dimensional spin arrangement and a competition between the strong spin coupling in the one-dimensional subsystem and weak three-dimensional interactions between the subsystems. Among Mn-containing oxides a large family of $\text{A}_{3m+3n}\text{A}'_n\text{Mn}_{3m+n}\text{O}_{9m+6n}$ hexagonal perovskites provide an example of an

extended investigation of the relationship between the magnetic properties and chemical composition.¹ These structures consist of infinite chains of face-shared MnO_6 octahedra with columns of A cations between the chains. Part of the octahedra can be replaced by $\text{A}'\text{O}_6$ ($\text{A}' = \text{Cu}, \text{Ni}, \text{Zn}, \text{Pd}, \text{Co}$)¹ trigonal prisms and the magnetic properties of these compounds are usually complex and depend on the type of the A' cation and on the sequence of MnO_6 octahedra and $\text{A}'\text{O}_6$ prisms along the chains.

* To whom correspondence should be addressed. E-mail: abakumov@icr.chem.msu.ru. Tel: (095) 939-52-44. Fax: (095) 939-47-88.

(1) Stitzer, K. E.; Darriet, J.; zur Loye, H.-C. *Curr. Opin. Solid State Mater. Sci.* **2001**, 5, 535.

Sb_2MnO_4 represents another example of quasi-1D structure containing infinite chains of edge-shared MnO_6 octahedra.^{2,3} These rutile-type $\{\text{MnO}_4\}_\infty$ chains are linked together by Sb atoms. Below $T_N = 60$ K this compound orders antiferromagnetically (AFM). The Mn^{2+} spins order AFM along the chain direction, but neighboring chains are ferromagnetically (FM) coupled.^{4,5} One of the possible ways to achieve chemical modification of the Sb_2MnO_4 structure arises from the similarity between the Sb_2MnO_4 and tetragonal Pb_3O_4 crystal structures.⁶ The latter can be represented as $\text{Pb}^{2+}_2\text{-Pb}^{4+}\text{O}_4$, where the Pb^{4+} cations are located in the centers of octahedra, and Pb^{2+} ones lie between the chains. The specific coordination environments of Pb^{2+} and Sb^{3+} cations comprising three oxygen atoms and a lone electron pair are virtually the same in both structures, which makes heterovalent replacement possible. In this contribution we describe the preparation, structure, and magnetic properties of the Pb-doped Sb_2MnO_4 -based complex oxides.

2. Experimental Section

The $(\text{Sb}_{1-x}\text{Pb}_x)_2(\text{Mn}_{1-y}\text{Sb}_y)\text{O}_4$ samples were prepared starting from PbO , Sb_2O_3 , MnO , Mn_2O_3 , and MnO_2 (Reakhim, "chemically pure" purity grade, Alfa Aesar, 99.99%). The amounts of initial reagents taken according to the required cation ratio, oxygen content, and overall sample weight of 0.5 g, were mixed under acetone and pressed into pellets. The pellets were placed into alumina crucibles and sealed under dynamic vacuum of $\sim 10^{-2}$ mbar into silica tubes with 12-mm diameter and ~ 60 -mm length. The samples were annealed at 650 °C for 50–100 h and then furnace-cooled.

The X-ray powder diffraction (XPD) investigation was performed with a focusing Guinier-camera FR-552 ($\text{CuK}\alpha_1$ radiation, Ge was used as an internal standard). XPD data for crystal structure determination were collected on a STADI-P diffractometer ($\text{CuK}\alpha_1$ radiation, curved Ge monochromator, transmission mode, linear PSD). The RIETAN-97 program package was used for the Rietveld refinement.⁷

Specimens for electron microscopy were prepared by crushing the samples in ethanol and depositing fragments on a holey carbon grid. Electron diffraction (ED) patterns and energy-dispersive X-ray (EDX) spectra were obtained in a Philips CM20 electron microscope with a LINK2000 attachment. EDX analysis was performed with $\text{Pb}(\text{M}\alpha)$, $\text{Sb}(\text{L}\alpha)$, and $\text{Mn}(\text{K}\alpha)$ lines. Pb_2MnO_4 and Sb_2MnO_4 were used as standards. High-resolution electron microscopy (HREM) observations were made on a JEOL4000EX instrument. Image simulations were carried out with the MacTempas software.

DC magnetic susceptibility measurements were performed with a Quantum Design MPMS-XL SQUID magnetometer with the applied field of 1000 Oe both in field cooled (FC) and zero-field cooled (ZFC) modes.

The transition metal L_3 -edge XANES measurements were performed on beam line X-19A and X-18B, at the Brookhaven National Synchrotron Light Source, which respectively have double crystal and channel cut Si (111) monochromators. Fluorescence and transmission mode measurements were made. The relative energies

between various spectra were determined using a simultaneous standard with the accuracy about ± 0.1 eV. All spectra were normalized to unity step in the absorption coefficient from well below to well above the edge.

Time-of-flight neutron powder diffraction (NPD) data were collected with the high-intensity powder diffractometer (HIPD) at the Los Alamos Neutron Science Center (LANSCE). Data were collected at room temperature, 90 K, and 20 K. High-resolution (at 153°, $\Delta d/d = 0.003$) and medium-resolution (at 90°, $\Delta d/d = 0.005$) data banks were used for the refinement of nuclear and magnetic structure, respectively. Diffractometer constants were refined with a $\text{Na}_2\text{Al}_2\text{Ca}_3\text{F}_{14}$ standard.⁸ Rietveld refinements were performed with the GSAS/EXPGUI suite.^{9,10}

3. Results and discussion

3.1 Sample Preparation and Characterization. The hypothesis about the existence of $(\text{Sb}_{1-x}\text{Pb}_x)_2\text{MnO}_4$ solid solutions was tested first. The samples with $0 \leq x \leq 0.75$, $\Delta x = 0.05$ were multiphase, but contained the compounds with Sb_2MnO_4 -type structure as the main constituent. These compounds show systematic variation of lattice parameters with changing lead content, which suggests that the solid solution is formed, with a composition deviating from the intended $(\text{Sb}_{1-x}\text{Pb}_x)_2\text{MnO}_4$. For $0.05 \leq x \leq 0.25$ the samples consisted of two Sb_2MnO_4 -type phases, with different lattice parameters. The lattice parameters of the first phase are nearly constant, whereas the second phase exhibits a decrease of the a parameter and an increase of the c parameter with increasing x . EDX spectra, taken from a large number of crystallites of these samples, can be divided into two sets: the cation ratio for the crystallites belonging to one set does not depend on the x value and is equal to $\text{Pb/Sb/Mn} = 0.66(7):1.54(5):0.80(5)$, whereas the crystallites of the other set show a systematic change of the composition from $\text{Pb/Sb/Mn} = 0.10(7):1.96(4):0.94(3)$ for $x = 0.1$ to $\text{Pb/Sb/Mn} = 1.56(4):0.92(4):0.52(1)$ for $x = 0.6$. For $x > 0.25$ MnO and Mn_2O_3 were found as admixtures, which indicates that the solid solutions are Mn-depleted. For $x > 0.6$ the $\text{Pb}_2\text{Sb}_2\text{O}_7$ pyrochlore and the $\text{Pb}_5\text{Sb}_2\text{MnO}_{11}$ compound¹¹ were found as impurities.

The EDX results indicate that the appropriate chemical formula for the solid solutions could be $(\text{Sb}_{1-x}\text{Pb}_x)_2(\text{Mn}_{1-y}\text{Sb}_y)\text{O}_4$, i.e., Mn at the B-site is partially replaced by Sb. This assumption was confirmed by the successful preparation of the single phase samples, listed in Table 1. A slight excess of oxygen in comparison with the nominal O_4 composition was needed to create the required equilibrium partial oxygen pressure inside the sealed silica tube. Samples prepared with nominal oxygen content contained metallic Pb as an impurity.

XPD patterns for the single phase $(\text{Sb}_{1-x}\text{Pb}_x)_2(\text{Mn}_{1-y}\text{Sb}_y)\text{O}_4$ samples were indexed on a tetragonal lattice with unit cell parameters listed in Table 1. The observed extinction

(2) Chater, R.; Gavarrı, J. R. *J. Solid State Chem.* **1985**, *59*, 123.

(3) Fjellvåg, H.; Kjekshus, A. *Acta Chem. Scand.* **1985**, *A39*, 389.

(4) Gavarrı, J. R.; Hewat, A. W. *J. Solid State Chem.* **1983**, *49*, 14.

(5) Gavarrı, J. R.; Calvarin, G.; Chardon B. *J. Solid State Chem.* **1983**, *47*, 132.

(6) Gavarrı, J. R.; Weigel, D. *J. Solid State Chem.* **1975**, *13*, 252.

(7) Izumi, F.; Ikeda, T. *Mater. Sci. Forum* **2000**, *198*, 321.

(8) Courbion, G.; Ferey, G. *J. Solid State Chem.* **1988**, *76*, 426.

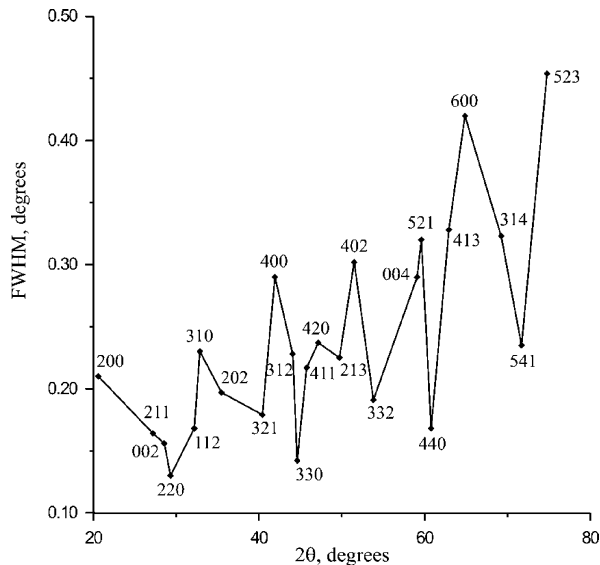
(9) Larson, A. C.; Von Dreele, R. B. *LAUR 86-748*. Los Alamos National Laboratory: Los Alamos, NM, 1994.

(10) Toby, B. H. *J. Appl. Crystallogr.* **2001**, *34*, 210.

(11) Abakumov, A. M.; Rozova, M. G.; Chizhov, P. S.; Antipov, E. V.; Hadermann, J.; Van Tendeloo, G. *J. Solid State Chem.* **2004**, *177*, 2855.

Table 1. Initial Sample Compositions and Unit Cell Parameters of the Single Phase Samples of the $(\text{Sb}_{1-x}\text{Pb}_x)_2(\text{Mn}_{1-y}\text{Sb}_y)\text{O}_4$ Solid Solutions

initial sample composition	a , Å	c , Å
Sb_2MnO_4	8.719(2)	5.999(2)
$\text{Pb}_{0.1}\text{Sb}_{1.96}\text{Mn}_{0.94}\text{O}_{4.05}$	8.7028(8)	6.001(1)
$\text{Pb}_{0.44}\text{Sb}_{1.64}\text{Mn}_{0.92}\text{O}_{4.1}$	8.6492(7)	6.088(1)
$\text{Pb}_{0.53}\text{Sb}_{1.58}\text{Mn}_{0.89}\text{O}_{4.1}$	8.6394(8)	6.118(1)
$\text{Pb}_{0.75}\text{Sb}_{1.48}\text{Mn}_{0.77}\text{O}_{4.1}$	8.6220(7)	6.1641(5)
$\text{Pb}_{0.85}\text{Sb}_{1.42}\text{Mn}_{0.73}\text{O}_{4.1}$	8.6168(5)	6.1818(6)
$\text{Pb}_{1.07}\text{Sb}_{1.26}\text{Mn}_{0.67}\text{O}_{4.1}$	8.6100(4)	6.2332(5)
$\text{Pb}_{1.186}\text{Sb}_{1.175}\text{Mn}_{0.639}\text{O}_{4.1}$	8.6110(8)	6.2462(9)
$\text{Pb}_{1.216}\text{Sb}_{1.155}\text{Mn}_{0.628}\text{O}_{4.1}$	8.6131(8)	6.2485(7)

**Figure 1.** Full width at half-maximum– 2θ plot for $\text{Pb}_{1.216}\text{Sb}_{1.155}\text{Mn}_{0.628}\text{O}_4$.

conditions $h0l$, $0kl$, $h,k \neq 2n$, hhl , $l \neq 2n$ are consistent with the space group $P4_2/mbc$. The a parameter decreases monotonically within the range $0 \leq x \leq 0.535$, and then increases slightly for $x = 0.593$, 0.608 . The c parameter increases with increasing x in the entire composition range. Closer examination of the XPD pattern taken with diffractometer from the $\text{Pb}_{1.216}\text{Sb}_{1.155}\text{Mn}_{0.628}\text{O}_4$ sample revealed a nonmonotonic variation of the peak widths with 2θ : reflections with significantly different values of h and k are stronger broadened (Figure 1). This can indicate an orthorhombic distortion. Le Bail fitting of the diffraction profile for the $\text{Pb}_{1.216}\text{Sb}_{1.155}\text{Mn}_{0.628}\text{O}_4$ sample with space group $Pbam$ gave slightly different values of the a and b parameters: $a = 8.5990(7)$ Å, $b = 8.6265(6)$ Å, $c = 6.2503(3)$ Å; the orthorhombic distortion parameter $\xi = (b_o - a_o/b_o + a_o) \approx 1.6 \times 10^{-3}$. However, no clear splitting of reflections, which can be attributed to orthorhombic distortion, was observed.

3.2 Crystal Structures of $\text{Pb}_{0.44}\text{Sb}_{1.64}\text{Mn}_{0.92}\text{O}_4$, $\text{Pb}_{0.75}\text{Sb}_{1.48}\text{Mn}_{0.77}\text{O}_4$, $\text{Pb}_{1.07}\text{Sb}_{1.26}\text{Mn}_{0.67}\text{O}_4$, and $\text{Pb}_{1.186}\text{Sb}_{1.175}\text{Mn}_{0.639}\text{O}_4$. The crystal structures of the representative members of the $(\text{Sb}_{1-x}\text{Pb}_x)_2(\text{Mn}_{1-y}\text{Sb}_y)\text{O}_4$ solid solution were refined from XPD data. Atomic coordinates for the initial step of the refinement were taken from the Sb_2MnO_4 crystal structure.² At the first step the occupancies of the cation positions were refined. The scattering factors of the cation positions $8h$ and $4d$ were set for occupation by only Sb and Mn, respectively, and the occupancy factors were refined at fixed atomic coordinates and atomic displacement parameters (ADPs).

This procedure showed that higher electron density should be assigned to both positions. For instance, the values $g(8h) = 1.22(1)\text{Sb}$ and $g(4d) = 1.29(1)\text{Mn}$ were obtained for the $\text{Pb}_{0.75}\text{Sb}_{1.48}\text{Mn}_{0.77}\text{O}_4$ crystal structure, which corresponds to 62.2 and 32.2 e^-/atom , respectively. Assuming the $8h$ position to be occupied by Pb and Sb, and the $4d$ to be occupied by Mn and Sb, one can assign the occupancy factors as $g(8h) = 0.36\text{Pb} + 0.64\text{Sb}$ and $g(4d) = 0.75\text{Mn} + 0.25\text{Sb}$ to yield the desired electron density. The compound composition can be derived then as $\text{Pb}_{0.72}\text{Sb}_{1.53}\text{Mn}_{0.75}\text{O}_4$, in satisfactory agreement with the nominal composition. For further refinement, the occupancy factors were slightly changed to satisfy the nominal compositions of the samples. The same procedure was applied for all other refined structures. The final refinement was performed in an isotropic approximation for the ADPs and with common ADPs for oxygen atoms. Preferred orientation along the $[001]$ direction was taken into account using the March–Dollase function. The crystallographic parameters, atomic coordinates, interatomic distances, and bond angles are listed in Tables 2, 3, and 4. The experimental, calculated, and difference XPD patterns for $\text{Pb}_{0.44}\text{Sb}_{1.64}\text{Mn}_{0.92}\text{O}_4$ and $\text{Pb}_{1.07}\text{Sb}_{1.26}\text{Mn}_{0.67}\text{O}_4$ are shown in Figure 2.

It should be noted that two diffuse, but clearly observable peaks at $d \approx 8.25\text{--}8.53$ Å and $d \approx 3.83\text{--}3.86$ Å are present in the XPD patterns of the $\text{Pb}_{1.07}\text{Sb}_{1.26}\text{Mn}_{0.67}\text{O}_4$, $\text{Pb}_{1.186}\text{Sb}_{1.175}\text{Mn}_{0.639}\text{O}_4$, and $\text{Pb}_{1.216}\text{Sb}_{1.155}\text{Mn}_{0.628}\text{O}_4$. These peaks do not originate from impurities, but can be attributed to cation ordering which is revealed from electron microscopy observations (see below). However, due to their significantly higher halfwidths, they cannot be used in the Rietveld refinement, and the narrow regions containing these broad peaks were excluded from the refinement.

The structure of the $(\text{Sb}_{1-x}\text{Pb}_x)_2(\text{Mn}_{1-y}\text{Sb}_y)\text{O}_4$ solid solutions resembles closely the parent Sb_2MnO_4 structure. It is built of infinite rutile-type chains of edge-shared distorted oxygen octahedra where Mn and part of Sb atoms are located (Figure 3a and b). The chains run along the c axis and are joined together by Pb or Sb atoms located between. Formally, the coordination environment of Pb/Sb atoms can be considered as a tetrahedron where two vertexes are formed by the O2 atoms of two neighboring $(\text{Mn}/\text{Sb})\text{O}_6$ octahedra; one vertex is the O1 atom of the neighboring chain and the fourth vertex is a lone electron pair oriented along the $\langle 110 \rangle$ direction (Table 4, Figure 3a).

Two competing trends—decreasing the average size of the cations in the Pb/Sb position and increasing the average cation size for the Mn/Sb site (according to the analysis of valence distribution below)—are compensated by the distortion of the $(\text{Mn}/\text{Sb})\text{O}_6$ octahedra, which in turn results in the variations of the a and c unit cell parameters in opposite directions. The Pb/Sb atom and two O2 atoms belonging to two neighboring $(\text{Mn}/\text{Sb})\text{O}_6$ octahedra are at the apexes of an isosceles triangle with two Pb/Sb–O2 bonds as edges and the O2–O2 separation as the base, aligned along the c axis (Figure 3c). The elongation of the Pb/Sb–O2 bonds does not significantly change the O2–Pb/Sb–O2 bond angle but increases the O2–O2 distance (see Table 4). This leads to a stretch along the c axis of the distorted square base of

Table 2. Selected Parameters from Rietveld Refinement of X-ray Powder Data for the $(\text{Sb}_{1-x}\text{Pb}_x)_2(\text{Mn}_{1-y}\text{Sb}_y)\text{O}_4$ Solid Solutions

	$\text{Pb}_{0.44}\text{Sb}_{1.64}\text{Mn}_{0.92}\text{O}_4$	$\text{Pb}_{0.75}\text{Sb}_{1.48}\text{Mn}_{0.77}\text{O}_4$	$\text{Pb}_{1.07}\text{Sb}_{1.26}\text{Mn}_{0.67}\text{O}_4$	$\text{Pb}_{1.186}\text{Sb}_{1.175}\text{Mn}_{0.639}\text{O}_4$
space group	$P4_2/mbc$	$P4_2/mbc$	$P4_2/mbc$	$P4_2/mbc$
a , Å	8.64111(8)	8.62028(9)	8.60767(8)	8.6126(1)
c , Å	6.07624(8)	6.1609(1)	6.23142(7)	6.2444(1)
Z	4	4	4	4
cell volume, Å ³	453.705(9)	457.81(1)	461.698(8)	463.19(1)
calcd density, g/cm ³	5.935	6.411	6.847	6.997
2θ range, step, deg.	$10 \leq 2\theta \leq 100$; 0.01	$10 \leq 2\theta \leq 110$; 0.01	$12 \leq 2\theta \leq 110$; 0.01	$12 \leq 2\theta \leq 110$; 0.01
number of reflections	134	164	165	165
refinable parameters	10	10	10	10
preferred orientation along the [001] axis	0.957(1)	0.966(2)	0.934(1)	0.891(2)
R_i , R_p , R_{wp}	0.014, 0.043, 0.056	0.012, 0.038, 0.051	0.017, 0.043, 0.058	0.015, 0.042, 0.059

Table 3. Positional Parameters, Occupancy Factors, and Atomic Displacement Parameters for the $(\text{Sb}_{1-x}\text{Pb}_x)_2(\text{Mn}_{1-y}\text{Sb}_y)\text{O}_4$ Solid Solutions

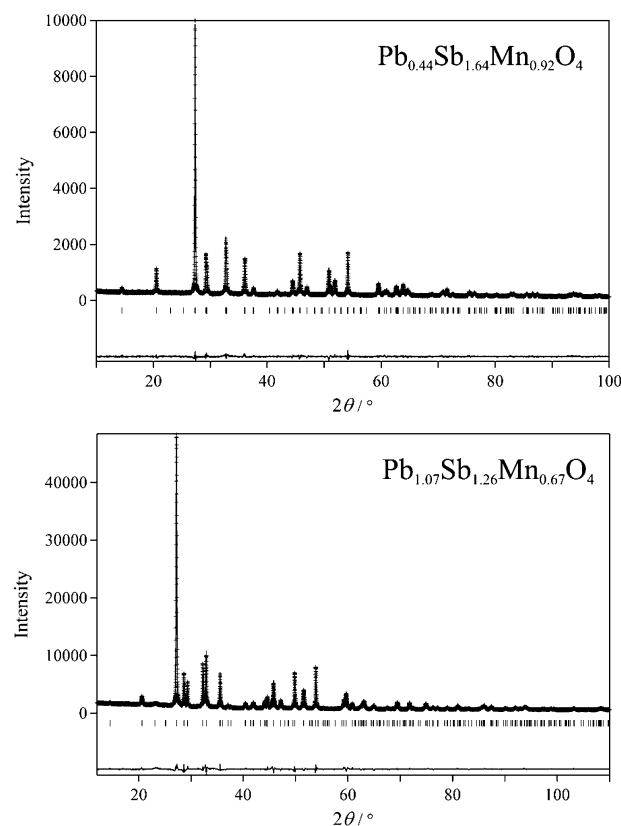
	$\text{Pb}_{0.44}\text{Sb}_{1.64}\text{Mn}_{0.92}\text{O}_4$	$\text{Pb}_{0.75}\text{Sb}_{1.48}\text{Mn}_{0.77}\text{O}_4$	$\text{Pb}_{1.07}\text{Sb}_{1.26}\text{Mn}_{0.67}\text{O}_4$	$\text{Pb}_{1.186}\text{Sb}_{1.175}\text{Mn}_{0.639}\text{O}_4$
Pb/Sb (x , y , 0) $8h$ x/a , y/b	0.1639(3), 0.1680(3)	0.1619(3), 0.1618(3)	0.1595(2), 0.1560(2)	0.1595(3), 0.1545(3)
B (Å ²), g (Pb/Sb)	1.65(3), 0.22/0.78	1.37(3), 0.375/0.625	1.61(2), 0.535/0.465	1.66(4), 0.593/0.407
Mn/Sb (0, $1/2$, $1/4$) $4d$				
B (Å ²), g (Mn/Sb)	0.23(6), 0.92/0.08	0.59(6), 0.77/0.23	0.30(5), 0.67/0.33	0.46(7), 0.639/0.361
O1 (x , y , 0) $8h$				
x/a , y/b	0.146(1), 0.4016(9)	0.142(1), 0.403(1)	0.130(1), 0.404(1)	0.130(1), 0.404(1)
B (Å ²)	1.1(1)	0.5(2)	1.3(2)	1.2(2)
O2 (x , $1/2+x$, $1/4$) $8g$				
x/a , B (Å ²)	0.1810(6), 1.1(1)	0.1809(8), 0.5(2)	0.1757(7), 1.3(2)	0.176(1), 1.2(2)

Table 4. Selected Interatomic Distances (Å) and Bond Angles (deg) for the $(\text{Sb}_{1-x}\text{Pb}_x)_2(\text{Mn}_{1-y}\text{Sb}_y)\text{O}_4$ Solid Solutions

	$\text{Pb}_{0.44}\text{Sb}_{1.64}\text{Mn}_{0.92}\text{O}_4$	$\text{Pb}_{0.75}\text{Sb}_{1.48}\text{Mn}_{0.77}\text{O}_4$	$\text{Pb}_{1.07}\text{Sb}_{1.26}\text{Mn}_{0.67}\text{O}_4$	$\text{Pb}_{1.186}\text{Sb}_{1.175}\text{Mn}_{0.639}\text{O}_4$
$d(\text{Mn/Sb}-\text{O1})$	$2.149(5) \times 4$	$2.141(7) \times 4$	$2.088(6) \times 4$	$2.090(9) \times 4$
$d(\text{Mn/Sb}-\text{O2})$	$2.212(8) \times 2$	$2.205(9) \times 2$	$2.138(9) \times 2$	$2.139(13) \times 2$
$d(\text{Pb/Sb}-\text{O1})$	$2.025(9) \times 1$	$2.084(10) \times 1$	$2.154(9) \times 1$	$2.166(14) \times 1$
$d(\text{Pb/Sb}-\text{O2})$	$2.029(4) \times 2$	$2.058(4) \times 2$	$2.114(4) \times 2$	$2.118(6) \times 2$
$d(\text{O1}-\text{O1})$	$3.039(15) \times 1$	$2.973(19) \times 1$	$2.782(18) \times 1$	$2.781(28) \times 1$
	$3.093(4) \times 2$	$3.129(4) \times 2$	$3.144(3) \times 2$	$3.150(4) \times 2$
$d(\text{O2}-\text{O2})$	3.0381(1)	3.0805(1)	3.1157(1)	3.1222(1)
$\angle(\text{O1}-\text{Mn/Sb}-\text{O1})$	$92.1(3), 90.0(3)$	$93.9(4), 88.0(4)$	$97.7(4), 83.5(4)$	$97.8(6), 83.4(6)$

the $(\text{Mn/Sb})\text{O}_6$ octahedra formed by the O1 atoms (Figure 3c). Since the $\text{Mn/Sb}-\text{O1}$ distances decrease at the same time, the square base becomes compressed along the O1–O1 edge lying in the a – b plane. This deformation is reflected by O1–Mn–O1 bond angles which exhibit increasing deviation from 90°. This compression is also consistent with the increasing length of the $\text{Pb/Sb}-\text{O1}$ bond. Elongation of the square base of the $(\text{Mn/Sb})\text{O}_6$ octahedra along the c axis and its compression in the a – b plane result in opposite variation of the a and c lattice parameters. The limiting point of this deformation occurs near $\text{Pb}_{1.186}\text{Sb}_{1.175}\text{Mn}_{0.639}\text{O}_4$ composition where the a parameter begins to increase. Perhaps further shortening of the O1–O1 separation becomes energetically unfavorable because of strong electrostatic repulsion, and it restricts the homogeneity range of the $(\text{Sb}_{1-x}\text{Pb}_x)_2(\text{Mn}_{1-y}\text{Sb}_y)\text{O}_4$ solid solutions.

3.3 Cations Valences in the $(\text{Sb}_{1-x}\text{Pb}_x)_2(\text{Mn}_{1-y}\text{Sb}_y)\text{O}_4$ Solid Solutions—XANES Study. In Figure 4 the Mn–K edge spectra of $\text{Pb}_{0.1}\text{Sb}_{1.96}\text{Mn}_{0.94}\text{O}_4$ and $\text{Pb}_{1.216}\text{Sb}_{1.155}\text{Mn}_{0.628}\text{O}_4$ along with those of MnO and LaMnO_3 standards are shown. The Mn–K main edge in such materials manifests a chemical shift that is sensitive to the Mn-valence, as illustrated by the substantial displacement of the LaMnO_3 spectrum to higher energy with respect to that of MnO. The steeply rising portion of the $(\text{Sb}_{1-x}\text{Pb}_x)_2(\text{Mn}_{1-y}\text{Sb}_y)\text{O}_4$ spectra crosses the MnO spectrum (see rectangular box in Figure 4) intermediate in its two-step onset. This coincidence is consistent with the $(\text{Sb}_{1-x}\text{Pb}_x)_2(\text{Mn}_{1-y}\text{Sb}_y)\text{O}_4$ compounds being in the formally

**Figure 2.** Experimental, calculated, and difference X-ray diffraction patterns for $\text{Pb}_{0.44}\text{Sb}_{1.64}\text{Mn}_{0.92}\text{O}_4$ and $\text{Pb}_{1.07}\text{Sb}_{1.26}\text{Mn}_{0.67}\text{O}_4$.

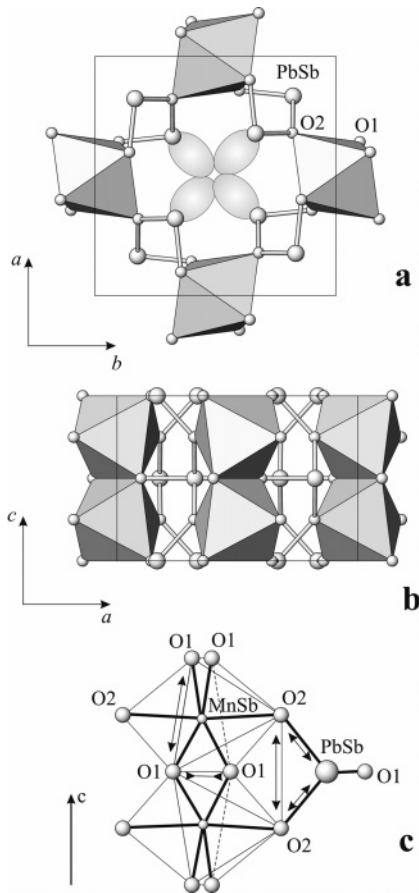


Figure 3. [001] (a) and [010] (b) projections of the $(\text{Sb}_{1-x}\text{Pb}_x)_2(\text{Mn}_{1-y}\text{Sb}_y)\text{O}_4$ structure. Mn/Sb atoms are located inside the octahedra. Orientation of lone electron pairs of the Pb/Sb cations is shown on the upper picture. (c) Coordination environment of the Pb/Sb and Mn/Sb cations. Variation of interatomic distances with increasing Pb content is schematically shown by arrows.

Mn^{2+} regime. Importantly, the overlaid spectra for the high and low Pb-content compounds show no systematic shift in the steeply rising portion of the edge. This indicates that very little shift in the Mn-valence, or covalency effects, accompany the Pb substitution and the concomitant Sb dual site occupancy. The spectrum of $\text{Pb}_{1.216}\text{Sb}_{1.155}\text{Mn}_{0.628}\text{O}_4$ is noticeably broadened due to the variation in the local environments of Mn in this material.

Further support for the Mn^{2+} state in these $(\text{Sb}_{1-x}\text{Pb}_x)_2(\text{Mn}_{1-y}\text{Sb}_y)\text{O}_4$ compounds can be found in the Mn-K pre-edge features shown in Figure 4. These pre-edge features are due to transitions into empty d -states allowed by $O-p/\text{Mn}-d$ hybridization. The pre-edge features of the $(\text{Sb}_{1-x}\text{Pb}_x)_2(\text{Mn}_{1-y}\text{Sb}_y)\text{O}_4$ compounds are extremely similar to that of MnO and much different from that of LaMnO_3 , confirming the Mn^{2+} state in these compounds.

The Sb- L_1 near edges involve transitions into the valence p -symmetry states above the Fermi energy. Consequently both the structure and chemical shift of the Sb- L_1 edge are good valence-state indicators. This is well illustrated in Figure 5a by the dramatic shift and spectral changes between Sb_2O_3 and Sb_2O_5 . The Sb- L_1 near edge of $\text{Pb}_{0.1}\text{Sb}_{1.96}\text{Mn}_{0.94}\text{O}_4$ is almost identical to that of Sb_2O_3 , confirming its Sb^{3+} character. In contrast, the Sb- L_1 near edge of the $\text{Pb}_{1.216}\text{Sb}_{1.155}\text{Mn}_{0.628}\text{O}_4$ appears to involve a strong Sb_2O_5 -like

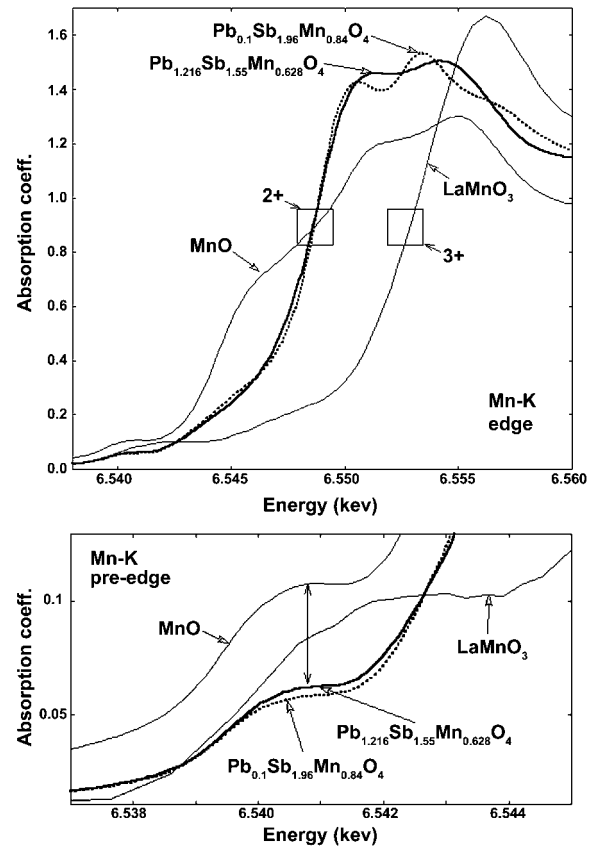


Figure 4. Top: the Mn-K edges of the $\text{Pb}_{0.1}\text{Sb}_{1.96}\text{Mn}_{0.94}\text{O}_4$ and $\text{Pb}_{1.216}\text{Sb}_{1.155}\text{Mn}_{0.628}\text{O}_4$ compounds along with those of the MnO and LaMnO_3 standards. The boxes indicate the regions where Mn^{2+} and Mn^{3+} spectra would be expected to fall in the absorption coefficient. Bottom: the Mn-K pre-edges of the $\text{Pb}_{0.1}\text{Sb}_{1.96}\text{Mn}_{0.94}\text{O}_4$ and $\text{Pb}_{1.216}\text{Sb}_{1.155}\text{Mn}_{0.628}\text{O}_4$ compounds along with those of the MnO and LaMnO_3 standards. The close similarity of the pre-edge structure of the spectra to that of MnO is emphasized by the double headed arrow.

component. This provides a very solid and direct confirmation that the Pb-substitution induces creation of Sb^{5+} . In Figure 5b a superposition of the Sb_2O_3 (with weight factor 0.3) and Sb_2O_5 (weight factor 0.7) spectra is used to simulate the $\text{Pb}_{1.216}\text{Sb}_{1.155}\text{Mn}_{0.628}\text{O}_4$ Sb- L_1 near edge. Although this superposition presumably overestimates the Sb^{5+} component substantially, because of the strong spectral intensity of the Sb_2O_5 spectrum in the vicinity of the Sb_2O_3 spectral peak, it serves to emphasize that in the $\text{Pb}_{1.216}\text{Sb}_{1.155}\text{Mn}_{0.628}\text{O}_4$ Sb- L_1 spectrum the Sb^{5+} component is very substantial.

It is reasonable to assume that the Pb/Sb position is occupied by Pb^{2+} and Sb^{3+} since both cations are too large to be octahedrally coordinated and have a lone electron pair necessary to complete their coordination environment ($r(\text{Pb}^{2+}) = 1.08 \text{ \AA}$, $r(\text{Sb}^{3+}) = 0.91 \text{ \AA}$).¹² Increasing Pb content results in a gradual increase of the average $\langle d(\text{Pb/Sb}-\text{O}) \rangle$ interatomic distance from 2.028 \AA for $\text{Pb}_{0.44}\text{Sb}_{1.64}\text{Mn}_{0.92}\text{O}_4$ to 2.134 \AA for $\text{Pb}_{1.186}\text{Sb}_{1.175}\text{Mn}_{0.639}\text{O}_4$, in agreement with the ionic radii of Pb^{2+} and Sb^{3+} . It is highly unlikely, however, that Sb^{3+} replaces Mn^{2+} in the octahedral sites, because such coordination environment is not typical for Sb^{3+} . The decreasing average $\langle d(\text{Mn/Sb}-\text{O}) \rangle$ distance from 2.170 \AA for $\text{Pb}_{0.44}\text{Sb}_{1.64}\text{Mn}_{0.92}\text{O}_4$ to 2.106 \AA for $\text{Pb}_{1.186}\text{Sb}_{1.175}\text{Mn}_{0.639}\text{O}_4$

(12) Shannon, R. D.; Prewitt, C. T. *Acta Crystallogr.* **1969**, B25, 925.

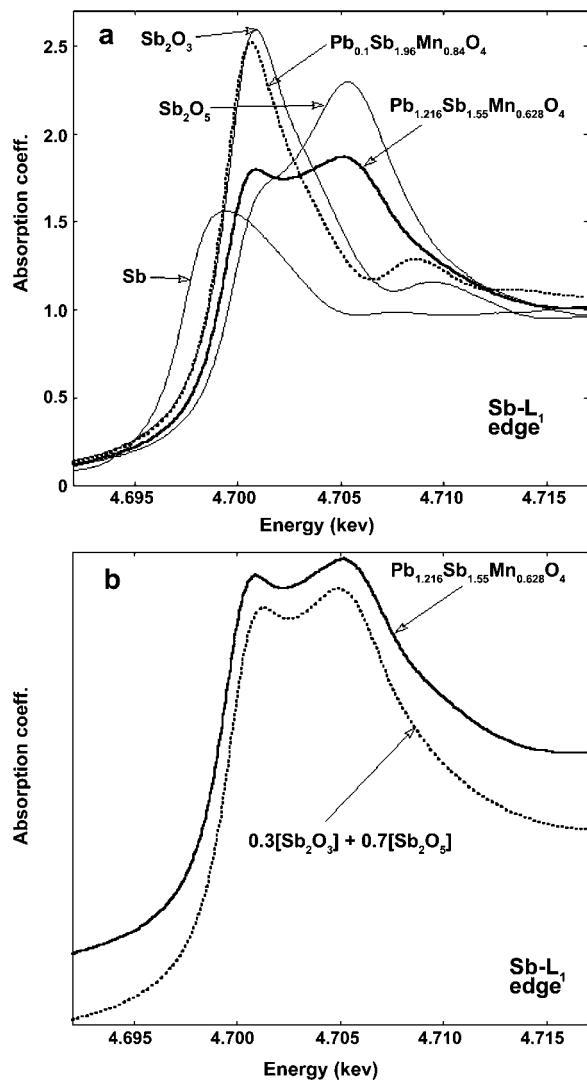


Figure 5. (a) Sb-L₁ edges of the Pb_{0.1}Sb_{1.96}Mn_{0.94}O₄ and Pb_{1.216}Sb_{1.155}Mn_{0.628}O₄ compounds along with those of the Sb, Sb₂O₃, and Sb₂O₅ standards. (b) Sb-L₁ edges of the Pb_{1.216}Sb_{1.155}Mn_{0.628}O₄ compounds compared to a simulated spectrum combining the Sb₂O₃ and Sb₂O₅ spectra with relative weights of 0.3 and 0.7, respectively.

indicates that Mn²⁺ ($r = 0.96 \text{ \AA}$) is replaced by a cation of smaller size, which can be Sb⁵⁺ ($r = 0.75 \text{ \AA}$). Thus, the idealized formula of the solid solutions can be written as (Sb³⁺_{1-x}Pb²⁺_x)₂(Mn²⁺_{1-y}Sb⁵⁺_y)O₄ with $x = 3/2y$ to maintain charge balance. However, the real compositions deviate slightly from the idealized ones, because the Mn oxidation state can exceed +2, as it is influenced by the partial oxygen pressure in the ampule, which cannot be precisely controlled in our preparations.

3.4 Electron Diffraction Study. For the samples with $x \leq 0.22$ the ED patterns show close resemblance to those of the basic Sb₂MnO₄ structure, as shown in Figure 6 for Pb_{0.1}Sb_{1.96}Mn_{0.94}O₄. These patterns can be indexed on a tetragonal lattice with $a \approx 8.70 \text{ \AA}$, $c \approx 6.05 \text{ \AA}$. The $0kl$, $k \neq 2n$, hhl , $l \neq 2n$ extinction conditions are consistent with $P4_2/mbc$ space symmetry. The reflections $0k0$ and $h00$ with $k, h \neq 2n$ on the [001]* ED pattern appear due to double diffraction as was confirmed by tilting experiments. Further changing of the composition results in the appearance of superlattice reflections. On the [100]* and $[\bar{1}10]^*$ ED patterns of Pb_{0.44}-

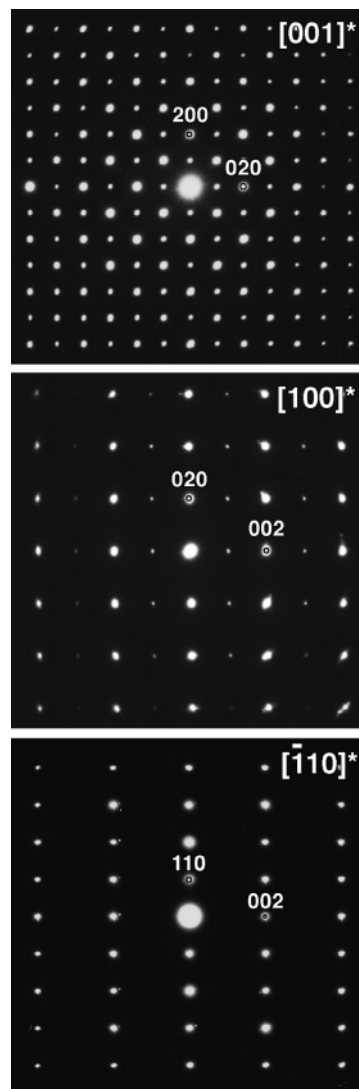


Figure 6. [001]*, [100]*, and $[\bar{1}10]^*$ ED patterns for Pb_{0.1}Sb_{1.96}Mn_{0.94}O₄.

Sb_{1.64}Mn_{0.92}O₄ very weak rows of diffuse intensity pass along the [001]* direction indicating the presence of short range order (Figure 7a and b). The ED patterns of Pb_{0.75}Sb_{1.48}Mn_{0.77}O₄ exhibit couples of vague satellites surrounding each basic reflection and aligned along [001]* (Figure 7c and d). For Pb_{0.85}Sb_{1.42}Mn_{0.73}O₄ (Figure 7e and f) and Pb_{1.216}Sb_{1.155}Mn_{0.628}O₄ (Figure 7g and h) the satellite reflections become sharper and more intense, and their position along the c^* axis changes with respect to the basic reflections. Indexing of the ED patterns of the Pb_{0.75}Sb_{1.48}Mn_{0.77}O₄, Pb_{0.85}Sb_{1.42}Mn_{0.73}O₄, and Pb_{1.216}Sb_{1.155}Mn_{0.628}O₄ compounds can be performed with a (3 + 1)-dimensional approach, assuming a modulation vector $\mathbf{q} = \gamma c^*$, where γ changes with the composition. The indexing scheme for the $02lm$ and $11lm$ reflection rows of the [100]* and $[\bar{1}10]^*$ ED patterns of Pb_{1.216}Sb_{1.155}Mn_{0.628}O₄ is shown in Figure 8a and b, respectively. The γ component of the \mathbf{q} vector was measured from the ED patterns as $\gamma = 0.603$ for Pb_{0.75}Sb_{1.48}Mn_{0.77}O₄, $\gamma = 0.671$ for Pb_{0.85}Sb_{1.42}Mn_{0.73}O₄, $\gamma = 0.726$ for Pb_{1.07}Sb_{1.26}Mn_{0.67}O₄, and $\gamma = 0.753$ for Pb_{1.216}Sb_{1.155}Mn_{0.628}O₄. Using the measured values of the γ components, the presence of broad reflections on the XPD patterns of the Pb_{1.07}Sb_{1.26}Mn_{0.67}O₄, Pb_{1.186}Sb_{1.175}Mn_{0.639}O₄, and Pb_{1.216}Sb_{1.155}Mn_{0.628}O₄

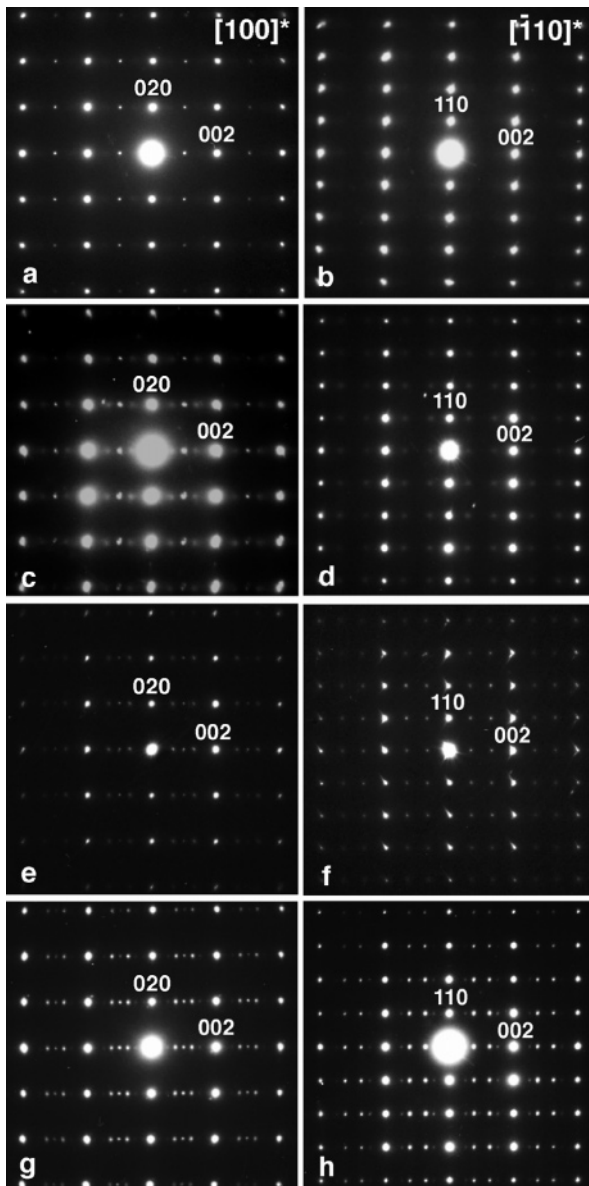


Figure 7. $[100]^*$ and $[\bar{1}10]^*$ ED patterns for $Pb_{0.44}Sb_{1.64}Mn_{0.92}O_4$ (a and b), $Pb_{0.75}Sb_{1.48}Mn_{0.77}O_4$ (c and d), $Pb_{0.85}Sb_{1.42}Mn_{0.73}O_4$ (e and f) and $Pb_{1.216}Sb_{1.155}Mn_{0.628}O_4$ (g and h).

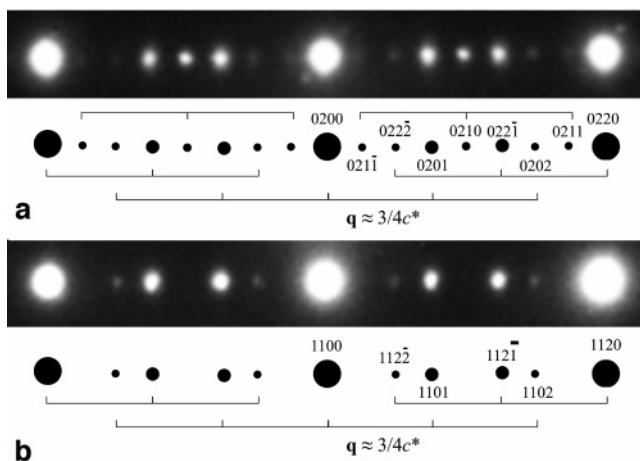


Figure 8. Indexation scheme for the $02lm$ and $11lm$ reflection rows of the $[100]^*$ (a) and $[\bar{1}10]^*$ (b) ED patterns of $Pb_{1.216}Sb_{1.155}Mn_{0.628}O_4$.

compounds can be explained. The position of the peak at $d \approx 8.25\text{--}8.53 \text{ \AA}$ corresponds to the 0001 reflection, whereas

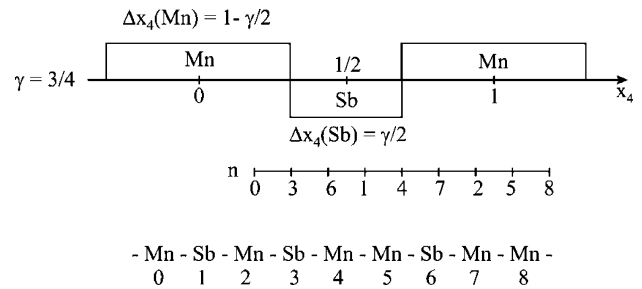


Figure 9. Positions of crenel domains for Mn and Sb atoms along the internal coordinate x_4 for $\gamma = 3/4$. The numbered discrete points correspond to the x_4 values ($x_4 = \gamma((1 + 2n)/4)$) associated with consecutive Mn/Sb layers along z . The resulting sequence of Mn and Sb layers is shown at the bottom.

the peak at $d \approx 3.83\text{--}3.86 \text{ \AA}$ is a result of overlap of the $11\bar{2}1$, 2100 , 2001 , and $211\bar{1}$ reflections. The γ components, calculated from the position of the 0001 reflection, are $\gamma = 0.7304$ for $Pb_{1.07}Sb_{1.26}Mn_{0.67}O_4$ and $\gamma = 0.7575$ for $Pb_{1.216}Sb_{1.155}Mn_{0.628}O_4$, in good agreement with those measured from ED data. From the $0klm$, $k \neq 2n$, $h0lm$, $h \neq 2n$, and $hhlm$, $l \neq 2n$ extinction conditions the superspace group can be derived as $P4_2/mbc(00\gamma)$. The symmetry of the $Pb_{1.216}Sb_{1.155}Mn_{0.628}O_4$ structure, taking into account weak orthorhombicity indicated by XPD, should be reduced to $Pbam(00\gamma)$. This $(3 + 1)D$ symmetry does not allow the $hhlm$, $l \neq 2n$ extinction conditions. However, according to the HREM observations described below, the cation ordering occurs in such a way that the intensity of the $hhlm$, $l \neq 2n$ is very close to zero, and these reflections do not show up on the experimental ED patterns.

3.5 HREM Investigation and the Model for Cation Ordering. The $Pb_{1.216}Sb_{1.155}Mn_{0.628}O_4$ sample was investigated by HREM because it shows more pronounced superlattice reflections in comparison with other samples. One may assume that the superstructure is caused by ordering of Mn and Sb atoms at the Mn/Sb positions resulting in layers occupied completely or preferentially either by Mn or by Sb atoms. The possible model for such ordering can be constructed applying the steplike crenel occupation function for the atoms in the Mn/Sb position. Taking into account the weak orthorhombicity of the $Pb_{1.216}Sb_{1.155}Mn_{0.628}O_4$ structure, the model was built in the $(3 + 1)D$ group $Pbam(00\gamma)$.

One Mn and one Sb atom with equal coordinates $0, 1/2, 1/4$ were introduced with the crenel domains centered at x_4 (Mn) = 0 and x_4 (Sb) = $1/2$ with $\Delta x_4(Mn) + \Delta x_4(Sb) = 1$ to keep the full occupancy of this position. From the two limiting cases of $\gamma = 0$ (Mn/Sb position is occupied by Mn atoms only, $\Delta x_4(Mn) = 1$) and $\gamma = 2$ (Mn/Sb position is occupied by Sb atoms only, $\Delta x_4(Sb) = 1$) and the repeat period of the modulation is equal to the distance between neighboring Sb layers, i.e., to $1/2c$, since there are two layers per average unit cell at $z = 1/4, 3/4$ the conditions $\Delta x_4(Mn) = 1 - \gamma/2$ and $\Delta x_4(Sb) = \gamma/2$ can be deduced. Figure 9 shows the arrangement of the crenel domains for a commensurate case of $\gamma = 3/4$. The sequence of Mn and Sb layers can be easily derived from the positions and widths of the crenel domains taking into account that the x_4 coordinate for each layer can be expressed as $x_4 = t + \gamma((1 + 2n)/4)$, where t is an initial "phase" of the modulation and n is the number of each successive layer. This simple picture can be

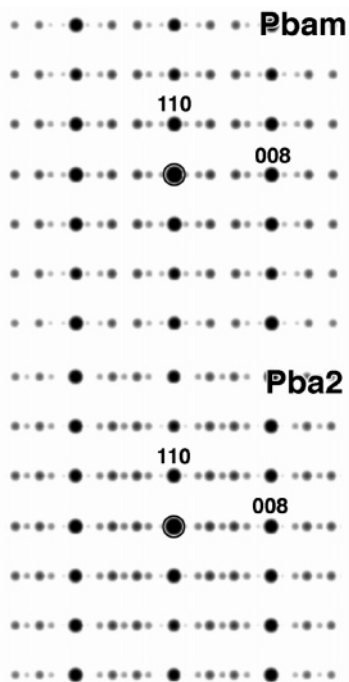


Figure 10. [110]* ED patterns for the *Pbam* and *Pba2* structures calculated at crystal thickness of 100 Å. Note the absence of the hhl , $l = 4n$, n – odd reflections on the pattern calculated with the *Pbam* model.

also applied for any other values of the γ component of the modulation vector. For $\gamma = 3/4$ (which is the nearest commensurate value for the $\text{Pb}_{1.216}\text{Sb}_{1.155}\text{Mn}_{0.628}\text{O}_4$ structure with $\mathbf{q} = 0.753c^*$) the *Pbam* space group can be derived for $t = p/4$, $(1 + 2p)/8$ (p is integer) and the *Pba2* space group for all other t values.

This model was verified by calculation of the theoretical ED patterns and HREM images. The atomic coordinates and occupancies were converted from the (3 + 1)D model into 3D supercell with $c = 4c_{\text{av}}$ and *Pbam* or *Pba2* space symmetries. The fully ordered sequence of Mn and Sb layers corresponding to those shown in Figure 9 can be realized in the space group *Pba2*, whereas the mirror planes of the *Pbam* space group at $z = 0, 0.5$ passing through the Pb/Sb layers require a statistical occupations for the layers with $z = 0.4375, 0.5625$ ($n = 3, 4$). A remarkable feature is present in the [110]* experimental patterns: being reindexed in the supercell, the [110]* ED pattern shows zero intensity for the hhl , $l = 4n$, n – odd reflections. Figure 10 shows the calculated [110]* ED patterns for the *Pbam* and *Pba2* structures at crystal thickness of 100 Å. The *Pba2* structure produces noticeable intensity at the hhl , $l = 4n$, n – odd positions, whereas these reflections vanish completely for the *Pbam* structure. Hence, the *Pbam* model is preferable on this basis. Clearly, this intensity vanishing is a consequence of the specific atomic arrangement and not related to the extinction conditions, which are the same for the two symmetries.

Consequently, the *Pbam* model was further used for HREM image simulations. The [100] HREM image in Figure 11 shows a typical part of the $\text{Pb}_{1.216}\text{Sb}_{1.155}\text{Mn}_{0.628}\text{O}_4$ crystallite. At these imaging conditions (as it was deduced from image simulations) the rectangular pattern of bright dots represents the projections of the Mn/Sb atomic columns. The

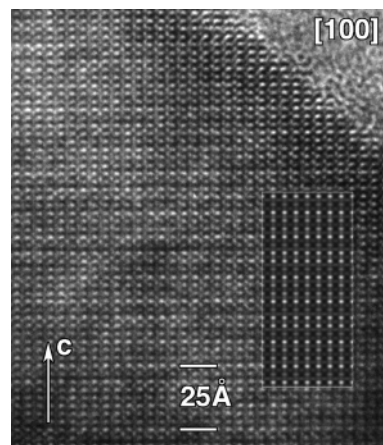


Figure 11. [100] HREM image of $\text{Pb}_{1.216}\text{Sb}_{1.155}\text{Mn}_{0.628}\text{O}_4$. The insert shows the theoretical image calculated at $\Delta_f = 200$ Å and $t = 100$ Å.

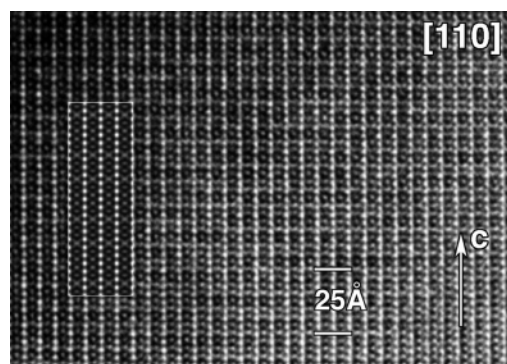


Figure 12. [110] HREM image of $\text{Pb}_{1.216}\text{Sb}_{1.155}\text{Mn}_{0.628}\text{O}_4$. The insert at left side of the picture shows the theoretical image calculated at $\Delta_f = -650$ Å and $t = 70$ Å.

superstructure manifests itself in the modulation of the intensity of the layers of dots along the c -direction, with an average repeat period of ~ 25 Å ($\approx 4c$). The theoretical image calculated at $\Delta_f = 200$ Å and $t = 100$ Å reproduces well the intensity variation in the dot rows and the sequence of alternation of the brighter and darker rows along the c axis. On the [110] HREM image (Figure 12) the superstructure is less visible, but can be recognized by alternation of dots with and without a dark halo around. The theoretical HREM image calculated with the *Pbam* model ($\Delta_f = -650$ Å and $t = 70$ Å) is also in agreement with the experimentally observed contrast.

The positions of Mn and Sb atoms in two neighboring layers are shifted by $\gamma/2$ along the a_4 direction; that means that two Sb layers cannot be placed next to each other when $\gamma \leq 1$. This is also in agreement with the HREM observations, which show that Sb layers are always separated at least by one Mn layer. One can deduce that this is driven by the requirement to keep the highly charged Sb^{5+} cations at maximal distances from each other along the c axis in order to minimize the electrostatic repulsion. The proposed model takes into account occupancy modulations only, which seem to have the main impact on the contrast in the HREM images. Clearly, occupancy modulations should be followed by displacement modulations, especially due to the different sizes and charges of Mn^{2+} and Sb^{5+} cations. However, HREM images do not provide enough experimental information to deduce the details of these modulations. The proposed

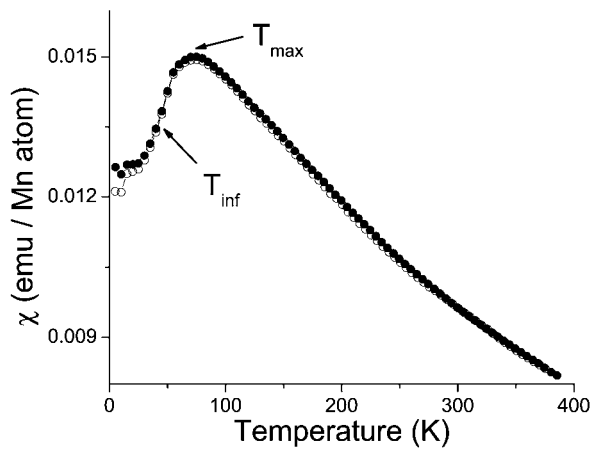


Figure 13. Temperature dependence of *dc* magnetic susceptibility (normalized per Mn atom) for $\text{Pb}_{0.10}\text{Sb}_{1.96}\text{Mn}_{0.94}\text{O}_4$. Filled and open symbols denote FC and ZFC data, respectively. Characteristic temperatures are marked with arrows.

model establishes the relationship between the Sb content at the Mn/Sb position and the γ component of the modulation vector as $\mathbf{g}_{\text{Sb}} = \gamma/2$. For $\text{Pb}_{1.216}\text{Sb}_{1.155}\text{Mn}_{0.628}\text{O}_4$ $\mathbf{g}_{\text{Sb}} = 0.372$, as given by the sample composition, agrees well with $\mathbf{g}_{\text{Sb}} = 0.377$ calculated from $\gamma = 0.753$. For the compounds with smaller Pb content the $\mathbf{g}_{\text{Sb}} = \gamma/2$ condition is not strictly satisfied due to incomplete ordering of Mn and Sb atoms. Indeed, the satellite reflections for these compounds are weak and diffuse, which can indicate a large degree of disorder. Large broadening of the 0001 reflections on the XRD patterns also supports this suggestion.

3.6 Magnetic Properties. The temperature dependence of magnetic susceptibility of the $\text{Pb}_{0.10}\text{Sb}_{1.96}\text{Mn}_{0.94}\text{O}_4$ sample exhibits a broad maximum at $T_{\text{max}} \approx 70$ K (Figure 13), characteristic of low-dimensional AFM systems. A Bonner–Fisher¹³ estimate of the magnitude of intrachain AFM exchange as $J_{\parallel} = T_{\text{max}}/1.282$ yields $J_{\parallel} \approx 55$ K. The transition temperature (T_{N}) to the 3D AFM state is associated with the inflection point (~ 45 K) on the $\chi(T)$ curve, and the interchain coupling $|J_{\perp}| = 6.3$ K was estimated with the expression¹⁴ $|J_{\perp}| = (T_{\text{N}}/1.28z[\ln(5.8J_{\parallel}/T_{\text{N}})]^{1/2})$ (where $z = 4$ is the number of neighboring chains). The $\xi = J_{\perp}/J_{\parallel}$ ratio, characterizing the “onedimensionality” of the system is $\xi = 0.11$, which is identical to that found in a similar quasi-1D pyroxene system NaVGe_2O_6 .¹⁵

Increasing Pb-doping induces the appearance of a discernible FM component in the magnetization: the $1/\chi$ vs T curves exhibit downturns at $T \approx 120$ K (Figure 14). The apparent independence of the transition temperature on x implies that the FM-like response may originate from a minor amount of unknown FM impurity which was not detected in the XPD patterns. However, a canted AFM state also cannot be excluded. The minor FM component refined from NPD data at 20 K of $\text{Pb}_{0.44}\text{Sb}_{1.64}\text{Mn}_{0.92}\text{O}_4$ (see below) stays equal to zero in the range of one standard deviation that favors an extrinsic reason for the magnetic anomaly at 120 K. The magnetic behavior below 120 K is complex and not

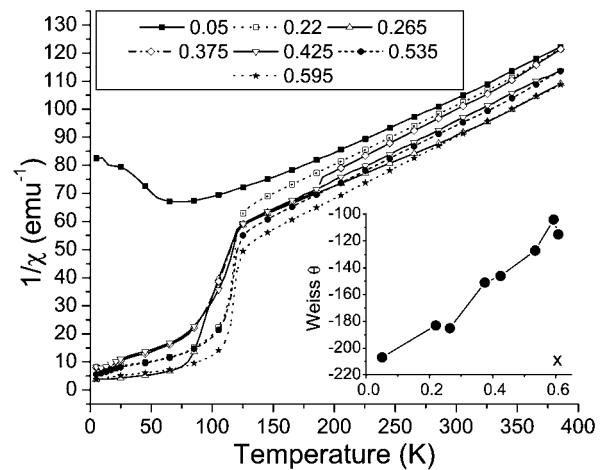


Figure 14. Temperature dependence of inverse *dc* magnetic susceptibility (normalized per Mn atom) for $(\text{Sb}_{1-x}\text{Pb}_x)_2(\text{Mn}_{1-y}\text{Sb}_y)\text{O}_4$ samples (ZFC). Inset: Weiss constant (θ) as a function of Pb content (x).

completely understood yet, especially because it could be a mixture of intrinsic and extrinsic contributions.

The paramagnetic susceptibility for all compounds except for $x = 0.05$ follows a regular Curie–Weiss (CW) law with the magnitude of the effective moment close to the theoretical values. For $\text{Pb}_{0.10}\text{Sb}_{1.96}\text{Mn}_{0.94}\text{O}_4$ CW asymptotics is also observed at $T \geq 200$ K, and the Weiss constant is $\theta = -207$ K, which is close to the value observed previously for Sb_2MnO_4 ($\theta = -190(20)$ K).³ The Weiss constant remains negative ($\theta < -100$ K) in the entire composition range, indicating that the dominant intrachain coupling is AFM. This is consistent with the Goodenough–Kanamori–Anderson rule for the 90° superexchange¹⁶ and earlier NPD findings on Sb_2MnO_4 .^{3–5} The $|\theta|$ decreases monotonically with increasing x (Figure 14) that reflects weakening of the intrachain AFM exchange induced by the “dilution” of Mn sublattice by a nonmagnetic entity (Sb^{5+}).

Low-temperature neutron diffraction experiments were performed on the $\text{Pb}_{0.44}\text{Sb}_{1.64}\text{Mn}_{0.92}\text{O}_4$ and $\text{Pb}_{1.186}\text{Sb}_{1.175}\text{Mn}_{0.639}\text{O}_4$ samples. In the case of $\text{Pb}_{1.186}\text{Sb}_{1.175}\text{Mn}_{0.639}\text{O}_4$, no magnetic intensity was detected down to 20 K. The possible minor ferromagnetic component ($\sim 0.02 \mu_{\text{B}}/\text{Mn}$ atom from *dc* magnetization data, assuming intrinsic origin of the 120 K anomaly) is too small to be reliably identified. For $\text{Pb}_{0.44}\text{Sb}_{1.64}\text{Mn}_{0.92}\text{O}_4$ at $T = 20$ K magnetic reflections are observed (Figure 15). Wollan–Koehler (WK) notation¹⁷ for the magnetic structures will be used here and subsequently. In this notation, three basic AF modes are denoted as “G” (both intrachain and interchain couplings are AFM), “C” (interchain coupling is AFM, and intrachain is FM), and “A” (intrachain coupling is AFM, and interchain is FM, see Figure 16), and “F” stands for the ferromagnetic mode. The observed magnetic reflections for $\text{Pb}_{0.44}\text{Sb}_{1.64}\text{Mn}_{0.92}\text{O}_4$ are consistent with the A-type magnetic structure: the most intense is the 110/001 doublet ($d \approx 6.1 \text{ \AA}$). The 001 reflection is the “forerunner” reflection of the A-type set, and 110 is an allowed nuclear reflection; the calculated nuclear intensity of the latter contributes $\sim 10\%$ of the total observed intensity.

(13) Bonner, J. C.; Fisher, M. E. *Phys. Rev.* **1964**, *135*, A640.

(14) Schulz, H. J. *Phys. Rev. Lett.* **1996**, *77*, 2790.

(15) Isobe, M.; Ueda, Y.; Vasiliev, A. N.; Voloshok, T. N.; Ignatchik, O. L. *J. Magn. Mater.* **2003**, *258–259*, 125.

(16) Goodenough, J. B. *Magnetism and the Chemical Bond*; Interscience Publishers: New York, 1963.

(17) Wollan, E. O.; Koehler, W. C. *Phys. Rev.* **1955**, *100*, 545.

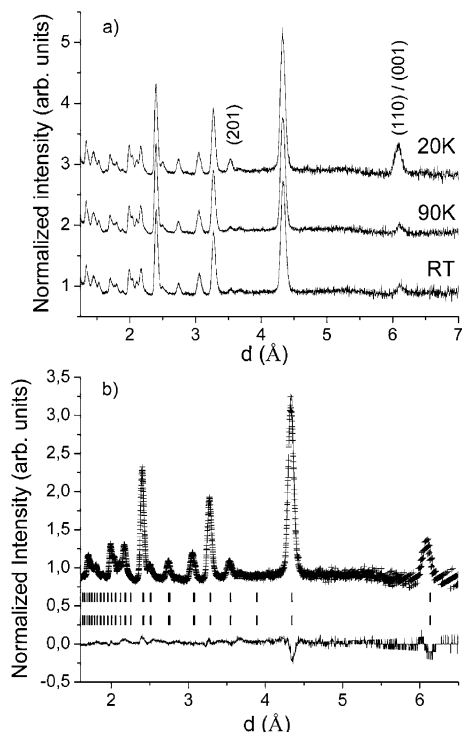


Figure 15. (a) Normalized neutron intensity data for $\text{Pb}_{0.44}\text{Sb}_{1.64}\text{Mn}_{0.92}\text{O}_4$ at room temperature, 90 K, and 20 K. Miller indices for main (A-type) magnetic reflections are shown. (b) Rietveld refinement of 20 K neutron diffraction data. Two sets of tick marks correspond to reflection positions in nuclear ($P4_2/mbc$, top) and magnetic ($Pb'2_1'm$, bottom) phases.

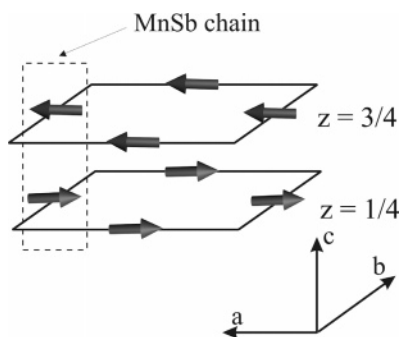


Figure 16. Schematic representation of the A_x antiferromagnetic structure. Note that any direction of the moment within xy (easy) plane is possible.

The intensity of both C- and G-type reflections is zero within the experimental error.

The symmetry-allowed spin configurations can be derived using group theory (Bertaut method).¹⁸ We consider only $k = 0$ (Γ point) structures (no evidence for a nonzero k -vector is observed in the ND data), and consequently adopt point group notations for the irreducible representations (irreps). The decomposition of magnetic (axial vector) representation for the $4d$ site of the $P4_2/mbc$ structure reads¹⁹ $\Gamma_{av} = B_{1g} + A_{2g} + 2E_g + B_{1u} + A_{2u} + 2E_u$, and the corresponding spin configurations are summarized in Table 5. The presence of two-dimensional irreps (E_g and E_u) in the decomposition implies that the Shubnikov symmetry approach, adopted in some of the previous works (e.g., ref 20) is intrinsically incomplete in the present case. Nevertheless, we retained

Shubnikov notations in Table 5 for the 1D irreps, to allow a direct comparison with those previous studies.

The magnetic structure of Sb_2MnO_4 was previously determined from neutron diffraction as mixed $A_{xy}A_z$ or $A_{xy}G_z$,^{3–5} with a dominant A_{xy} component in both cases. The alignment of the ordered moment in the ab plane (easy plane anisotropy) is indeed favored by the magnetodipolar energy, as shown by the calculation for the two limiting sets of lattice parameters for minimum and maximum Pb doping levels (see Table 6, the details on the magnetodipolar energy calculation are given in the Appendix). The change in lattice parameters does not have a significant effect on the magnetodipolar energy, and hence the majority spin component is expected to be confined in the ab plane for the entire doping range in $(\text{Sb}_{1-x}\text{Pb}_x)_2(\text{Mn}_{1-y}\text{Sb}_y)\text{O}_4$ solid solutions.

The E_g and E_u can yield relevant spin configurations with arbitrary direction of the magnetic moment within the (ab) plane. The observed negative θ is only consistent with A and G structures, i.e., with dominant AFM intrachain coupling, and weaker FM or AFM interchain interactions, respectively, and this leaves E_u irrep (corresponding to $(G/A)_{xy}$ spin structure, in modified WK notations of ref 19) as the most likely candidate.

The detailed neutron diffraction study of the related $\text{Sb}_2\text{-FeO}_4$ compound²⁰ revealed the presence of three AFM modes (A, G, and C), which requires a mixture of irreps if $P4_2/mbc$ symmetry is retained. Consequently, the authors of ref 20 considered orthorhombic distortion, as it was further evidenced by the anisotropic broadening of reflections in their NPD data. They found $Pmc2_1$ Shubnikov (and, hence, $Pmc2_1$ crystallographic) symmetry, and their model was later confirmed by a Mössbauer study.²¹ However, it is noteworthy that the symmetry reduction does not follow from purely symmetry considerations: a secondary order parameter (OP) for the transition driven by E_u irrep can also have B_{1g} symmetry. If this secondary OP is considered a magnetic one, this yields the admixture of a C_z mode, and the resultant structure is the one observed in ref 20.

The magnetic contribution to the ND pattern of the $\text{Pb}_{0.44}\text{-Sb}_{1.64}\text{Mn}_{0.92}\text{O}_4$ at $T = 20$ K can be adequately fitted by a simple A_{xy} model ($\chi^2 = 6.37$, $R_p = 2.79\%$, Figure 15b), which is consistent with tetragonal symmetry (as discussed above). An attempt to refine the minority FM component (assuming orthorhombic distortion and $Pb'2_1'm$ Shubnikov symmetry, which allows F_z spin component) did not yield any improvement in the reliability factors, and the refined value is $\mu_z = 0.2(3)\mu_B$. The refined (A_{xy}) ordered moment at 20 K is $2.63\text{--}(3)\mu_B$, which is substantially lower than the expected value ($0.92 \times 5 = 4.60\mu_B$), probably because at this temperature the magnetic moment is not yet saturated.

The observed A_{xy} structure does not allow the admixture of a FM component within $P4_2/mbc$ symmetry, but it becomes allowed in the $Pmc2_1$ subgroup (Table 5, where nonstandard $Pb2_1m$ setting is used to retain tetragonal axes). The $Pmc2_1$ in two nonstandard settings can appear as a result of a group—maximum subgroup tree: $P4_2/mbc \rightarrow Pbam \rightarrow$

(18) Bertaut, E. F. *Acta Crystallogr.* **1968**, *A24*, 217.

(19) Sivardiere, J. *Acta Crystallogr.* **1970**, *A26*, 101.

(20) Gonzalo, J. A.; Cox, D. E.; Shirane, G. *Phys. Rev.* **1966**, *147*, 415.

(21) Varret, F.; Imbert, P.; Gerard, A.; Hartmann-Boutron, F. *Solid State Commun.* **1968**, *6*, 889.

Table 5. Allowed Spin Configurations (in WK notation), Corresponding Irreps, and Shubnikov Groups (for 1D irreps) for the $P4_2/mbc$, $Pbam$, and $Pb2_1m$ ($Pmc2_1$) Symmetries with Magnetic Atom (Mn) at 4d $(\frac{1}{2}, 0, \frac{1}{4})$ Position of $P4_2/mbc$, at 4f $(\frac{1}{2}, 0, z)$ of $Pbam$, and at 4c (x, y, z) of $Pb2_1m$

$P4_2/mbc^a$			$Pbam$			$Pb2_1m$		
irrep	Shubnikov group	spin arrangement	irrep	Shubnikov group	spin arrangement	irrep	Shubnikov group	spin arrangement
A_{2g}	$P4_2/m'b'c'$	F_z	A_g	$Pbam$	C_z	A_1	$Pb2_1m$	A_x, G_y, C_z
A_{2u}	$P4_2/m'bc$	G_z	B_{3u}/B_{2u}	$Pb'am/Pba'm^b$	$(G/A)_{xy}$	B_2	$Pb'2_1'm$	G_x, A_y, F_z
B_{1g}	$P4_2'/mbc'$	C_z	B_{1u}	$Pbam'$	G_z	B_1	$Pb2_1'm'$	F_x, C_y, G_z
B_{1u}	$P4_2'/m'b'c$	A_z	B_{1g}	$Pb'a'm$	F_z	A_2	$Pb'2_1m'$	C_x, F_y, A_z
E_g		$(F/C)_{xy}$	B_{3g}/B_{2g}	$Pba'a'm'/Pb'am'^b$	$(F/C)_{xy}$			
E_u		$(G/A)_{xy}$	A_u	$Pb'a'm'$	A_z			

^a For $P4_2/mbc$, only irreps with at least one allowed spin component are shown. ^b Those configurations correspond to the same magnetic group as discussed in ref 18: they can be transformed into each other by an interchange of x and y axes.

$Pb2_1m$ (or, equivalent $P4_2/mbc \rightarrow Pbam \rightarrow P2_1am$). Group theory shows that the $Pmc2_1$ structure appears as isotropy subgroup of $P4_2/mbc$ corresponding to the E_u representation;²² hence, a single $P4_2/mbc \rightarrow Pmc2_1$ transition is also possible, and it is allowed to be continuous by both Landau and renormalization group theories.²² The orthorhombic distortion could thus provide an intrinsic mechanism for the observed weak ferromagnetism. However, no direct evidence for crystallographic symmetry lowering (neither for the FM component) was observed in the neutron diffraction data at low T . The refinements of the $\text{Pb}_{0.44}\text{Sb}_{1.64}\text{Mn}_{0.92}\text{O}_4$ data in the “relevant” orthorhombic subgroups yielded only marginal improvement in the fit quality (20 K, $P4_2/mbc$: $\chi^2 = 2.04$, $R_p = 1.42\%$; $Pbam$, $\chi^2 = 1.94$, $R_p = 1.38\%$; $Pb2_1m$, $\chi^2 = 1.87$, $R_p = 1.34\%$), while requiring a substantially larger number of parameters. The refined magnitude of the orthorhombic distortion is also extremely small: $\xi = (b_o - a_o/b_o + a_o) = 5 \times 10^{-4}$ at 20 K. NPD data on $\text{Pb}_{1.186}\text{Sb}_{1.175}\text{Mn}_{0.639}\text{O}_4$ show broad superlattice peaks associated with the modulated superstructure ($\gamma \approx \frac{3}{4}$). The spectrum (bank 1 data, where no visible superlattice peaks are present) can be adequately fit with the tetragonal $P4_2/mbc$ model ($\chi^2 = 1.63$, $R_p = 1.54\%$). The refinement revealed an anomalously high ADP for the Mn/Sb site ($B_{\text{iso}} = 2.9(9) \text{ \AA}^2$), which can be related to the joint occupation of this position by two cations with different properties, and concomitant atomic displacements. No attempt of the superstructure refinement was undertaken because of the limited number of superlattice reflections and limited resolution of the data.

4. Conclusions

Single phase samples of $(\text{Sb}_{1-x}\text{Pb}_x)_2(\text{Mn}_{1-y}\text{Sb}_y)\text{O}_4$ ($0.0 \leq x \leq 0.608$, $0.0 \leq y \leq 0.372$) solid solutions were synthesized. Combination of XPD, XANES, ED, HREM, and EDX analyses showed that substitution of Pb for Sb results in the oxidation of part of Sb^{3+} to Sb^{5+} , which in turn replace the Mn^{2+} cations in octahedrally coordinated positions within the infinite chains. The idealized formula for the solid solutions can be written as $(\text{Sb}^{3+}_{1-x}\text{Pb}^{2+}_x)_2(\text{Mn}^{2+}_{1-y}\text{Sb}^{5+}_y)\text{O}_4$ with $x = \frac{3}{2}y$, but the actual compositions deviate from the idealized ones due to slight variation of the Mn oxidation state, which nevertheless remains close to +2. Starting from

Table 6. Calculated Magnetodipolar Energies for Two Limiting Sets of Lattice Parameters: Top Row, $a = 8.719 \text{ \AA}$, $c = 5.999 \text{ \AA}$; Bottom Row, $a = 8.6131 \text{ \AA}$, $c = 6.2485 \text{ \AA}$

configuration (WK)	energy, meV
A_z	1.337
	1.213
G_z	1.251
	1.104
$A_x (= A_y)$	-0.668
	-0.607
$G_x (= G_y)$	-0.625
	-0.552

^a Moment of $5\mu_B$ is assigned to each B-site.

the $\text{Pb}_{0.75}\text{Sb}_{1.48}\text{Mn}_{0.77}\text{O}_4$ composition the ordering of Mn^{2+} and Sb^{5+} ions was observed by electron diffraction resulting in a modulated superstructure with $q = \gamma c^*$. HREM observations revealed that the Mn^{2+} and Sb^{5+} ions order by forming layers of octahedrally coordinated positions. The dilution of the magnetic Mn^{2+} sublattice by nonmagnetic Sb^{5+} ions leads to a suppression of the AFM intrachain interactions. Similar to the Sb_2MnO_4 parent compound, the A_{xy} spin component was found to be dominant in the AFM structure at low doping level ($x = 0.22$).

Acknowledgment. We are grateful to O. I. Lebedev for his useful contribution in the electron microscopy investigation and to E. Caspi, H. Stokes, R. Usmanov, and S. Vakhruhev for insightful conversations. We are also grateful to an unnamed referee for very helpful comments concerning the symmetry of magnetic and ferroelectric configurations. The work was supported in part by the program IAP V-1 of the Belgium government. Work at Rutgers was supported by the National Science Foundation grant DMR 02-33697. A.M.A. is grateful to the RFBR (04-03-32785a), to the INTAS for the Fellowships grant for Young Scientists YSF 2002-48 and YSF-05-55-1035 and to the Russian Science Support Foundation for the financial support.

Supporting Information Available: Crystallographic information files for the subject solid solutions (CIF). This material is available free of charge via the Internet at <http://pubs.acs.org>.

Appendix. Calculation of Magnetodipolar Energy.

Magnetic dipolar energy

$$E = -\frac{1}{2} \sum_{i \neq j} \frac{3(\mathbf{r}_{ij} \mu_i)(\mathbf{r}_{ij} \mu_j) - r_{ij}^2 (\mu_i \mu_j)}{r_{ij}^5} \quad (1)$$

is a double sum over all magnetic moments μ_i in the infinite lattice. It is expressed in terms of a single sum

(22) Stokes, H. T.; Hatch, D. M. *Isotropy Subgroups of the 230 Crystallographic Space Groups*; World Scientific: River Edge, NJ, 1988. The “Isotropy” software implementation is available at www.physics.byu.edu/~stokesh/findsymb.html.

$$E = -\frac{1}{2} \sum_i \mu_i F_i \quad (2)$$

where the fields

$$F_i = \sum_{j \neq i} \frac{3\mathbf{r}_{ij}(\mathbf{r}_{ij}\mu_j) - r_{ij}^2\mu_j}{r_{ij}^5} \quad (3)$$

were computed using the Ewald summation method to avoid truncation effects. The Ewald method gives²³

$$F_i^\alpha = \sum_j v_{\alpha\beta}(\mathbf{r}_{ij})\mu_j^\beta + \sum_{j \neq i} v_{\alpha\beta}(\mathbf{r}_{ij})\mu_j^\beta \quad (4)$$

where the summation is only over the moments within a single unit cell, $v_{\alpha\beta}(\mathbf{r}) = \partial^2 v / \partial r^\alpha \partial r^\beta$, $v_{\alpha\beta}(\mathbf{r}) = \partial^2 v(\mathbf{r}) / \partial r^\alpha \partial r^\beta$, $v(\mathbf{r}) = 1/r$, and $\nu(\mathbf{r})$ is the Madelung sum for the contribu-

tions of all other unit cells. The function $\nu(\mathbf{r})$ can be expressed as a fast converging series

$$\nu(\mathbf{r}) = -\frac{2\pi r^2}{3v_c} - \frac{\text{erf}(Gr)}{r} + \sum_{l \neq 0} \frac{1 - \text{erf}(G|\mathbf{r} - l|)}{|\mathbf{r} - l|} - \frac{\pi}{v_c G^2} + \frac{\pi}{v_c G^2} \sum_{\mathbf{g} \neq 0} \frac{\exp(-g^2/4G^2)}{g^2/4G^2} \cos(\mathbf{g}\mathbf{r}) \quad (5)$$

Here the sums are over the direct and reciprocal lattice vectors l and \mathbf{g} , v_c is the unit cell volume, and G is an arbitrary number (the Ewald's parameter), which affects convergence but not the result; a reasonable choice is $G = (\pi^2/v_c)^{1/3}$. The function $\nu(\mathbf{r})$ is regular within the unit cell $l = 0$, including the point $\mathbf{r} = 0$, and is not periodic because of the missing term. $\nu(\mathbf{r}) + 1/r$ is periodic in \mathbf{r} . The derivatives $v_{\alpha\beta}$ are evaluated analytically term-wise before the summation.

(23) Tsiper, E. V.; Soos, Z. G. *Phys. Rev.* **2001**, *B64*, 195124.